JOURNAL OF MATERIALS SCIENCE **35** (2000) 5371–5381

Multi-length scale modeling of CVD of diamond

Part II *A combined atomic-scale/grain-scale analysis*

M. GRUJICIC, S. G. LAI
Program in Materials Science and Engineering, Department of Mechanical Engineering, 241 Fluor Daniel Building, Clemson University, Clemson, SC 29634-0921
E-mail: mica@ces.clemson.edu

Chemical vapor deposition of polycrystalline diamond films is studied by combining an atomic-scale kinetic Monte Carlo model with two (one three-dimensional and one two-dimensional) grain-scale models. The atomic-scale model is used to determine the growth rates of (111)- and (100)-oriented surface facets, the surface morphology of the facets and the extent of incorporation of the crystal defects. Using the atomic-scale modeling predicted growth rates for the (111)- and (100)-oriented facets, grain-scale modelling is carried out to determine the evolution of grain structure, surface morphology and crystallographic texture in the polycrystalline diamond films. It is found that depending on the relative growth rates of the (111)- and (100)-oriented facets, which can be controlled by selecting the CVD processing conditions, one can obtain either ⟨110⟩-textured films with a relatively smooth faceted surface or ⟨100⟩-textured films with a highly pronounced deep facets. In both cases, however, the film surface is composed entirely of the ⟨111⟩ facets. This findings are found to be fully consistent with the available experimental results.

1. Introduction

Over the last decade, chemical vapor deposition (CVD) of the diamond films from a precursor gas mixture containing a small amount of hydrocarbon (e.g. CH_4, C_2H_2, etc.) and H_2 as the carrier gas at pressures in the range 1–200 Torr has become a commercially viable process [e.g. 1–3]. In the CVD process the gas mixture is heated via hot filaments, plasmas or combustion flames, to promote dissociation of the molecular hydrogen (H_2) into atomic hydrogen (H) and formation of various hydrocarbon radicals. While under the typical CVD processing conditions graphite is thermodynamically more stable than diamond, H atoms bond with and passivate the surface carbon atoms by converting the graphite-type sp^2-bonding into the diamond-type sp^3-bonding [2, 3].

It is well-established that CVD of the diamond occurs by incorporation of the chemisorbed hydrocarbon radicals. However, the mechanism of the diamond growth is still not well understood, primarily because the atomic-scale events which lead to diamond growth are difficult to study *in situ*. Consequently, computer modeling/simulations and/or interpretation of the *ex situ* experimental results are the main means of elucidating the mechanisms of diamond growth. A variety of modeling techniques have been employed to date. In a number of these models [e.g. 4, 5], the CVD process is analyzed at the reactor scale by solving the appropriate continuum reactive-gas fluid-dynamics/heat-transfer boundary value problem. While such models are quite useful in the design of CVD reactors and typically predict reasonably well the average film-growth rate, they can not account for the effect of surface morphology on the growth rate or be used to predict formation of the crystal defects during film deposition. In other classes of models, the CVD process is analyzed at the atomic scale. Among these models some deal with the surface energetics [6, 7], determination of kinetic parameters for individual surface reactions [7–9] and the analysis of stability of various surface configurations [10–16]. In addition, molecular dynamics [e.g. 17] and Monte Carlo [e.g. 18, 19] methods are utilized to carry out the three-dimensional atomic-scale simulations of CVD of the diamond single-crystalline films. The atomic-scale models, while being very instrumental in predicting the generation of crystal defects, and the effect of surface morphology on the film-deposition rate, can not be used to study the evolution of grain structure, surface morphology and texture in polycrystalline diamond films. While the latter phenomena can be analyzed using one of the grain-scale models such as the model proposed by Van der Drift [20], these models have not yet been applied to CVD of the polycrystalline diamond films.

In the present paper, which is Part II of a two-part paper, a multi-length scale approach is used to study CVD of the polycrystalline diamond films. In Part I [21], the CVD process is analyzed by coupling a reactor-scale model within which an appropriate reactor-scale continuum-type boundary value problem for reactive-gas mixture interacting with the deposition surface is combined with a kinetic Monte Carlo atomic-scale model. The coupling between the two models

is accomplished by: (a) using the species concentrations at the deposition surface obtained via the reactor-scale modeling to define the boundary conditions for the atomic-scale modeling and; (b) using the atomic-scale modelling results to identify which surface reactions govern CVD of the diamond single crystals of different crystallographic orientations and feed this information back into the reactor-scale model to ensure self consistency. In this paper, the atomic scale model developed in Part I [21], is coupled with two grain-scale models to study the evolution of surface morphology, grain structure and crystallographic and morphological textures in the polycrystalline diamond films.

The organization of the paper is as following: In Section II, a detailed description is given of the atomic-scale kinetic Monte Carlo method and of the results obtained by applying this method to CVD of the (111)- and (100)-oriented diamond single crystals. A simple three-dimensional and a two-dimensional grain-scale models for the evolution of grain-structure and film texture are developed and applied to study CVD of the polycrystalline diamond films in Section III. Main conclusions resulting from the present work are summarized in Section IV.

2. Atomic-scale modeling of CVD

2.1. General consideration

The growth of (111)- and (100)-oriented diamond films by the CVD has been modeled at the atomic scale using rigid diamond-type lattices. In other words, the atomic relaxations and vibrations are not considered. In the case of (111)-oriented films, the orientation of the lattice is defined as: $x = [11\bar{2}]$, $y = [1\bar{1}0]$ and $z = [111]$ while in the case of the (100)-oriented diamond films the lattice orientation is defined as $x = [011]$, $y = [0\bar{1}1]$, $z = [100]$. Each film is allowed to grow in the z-direction while periodic boundary conditions are applied in the x and y directions in order to avoid the film-edge effects. The size of the computational lattice in the x–y plane is $90\, d_{(112)} \times 40\, d_{(110)}$ for the (111)-oriented diamond film and $60\, d_{(011)} \times 40\, d_{(011)}$ for the (100)-orientated where $d_{(uvw)}$ is the spacing of the (uvw) diamond planes. Initially, six (111) and six (100) planes of the diamond lattice are filled with carbon atoms to form a six-layer thick (111) and a six-layer thick (100) substrate, respectively. To passivate the top layer of the substrates, the substrates are terminated with a layer of atomic hydrogen (H). Since the two substrates are shown in Fig. 1 of Part I [21] of this two-part paper, they are not reproduced here. However, Figs 1 and 2 in this paper can be used to obtain the information about the crystallographic orientations of the two substrates.

The growth of diamond requires that the hydrogen-terminated substrate surface be activated which can take place either by desorption or by abstraction of the chemisorbed atomic hydrogen. Once a substrate surface site is activated, it can be repassivated by chemisorption of either an atomic hydrogen or a hydrocarbon molecule. The chemisorbed hydrocarbon molecule can desorb and thus reactivate the site. Conversely, the

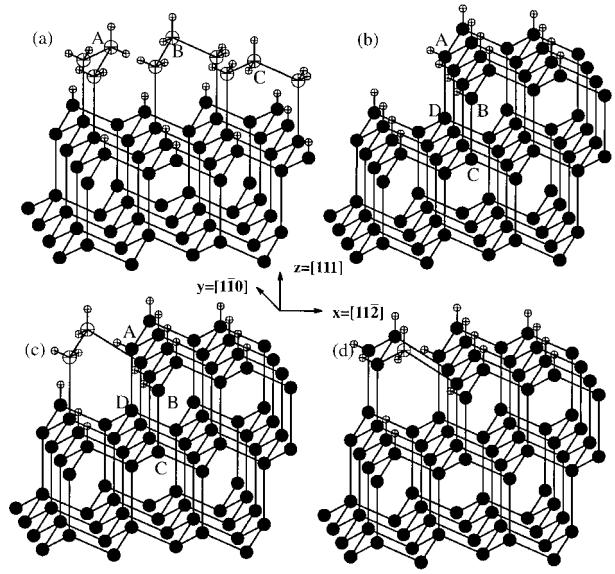

Figure 1 Formation of three equivalent three-carbon bridges, (a), whose growth leads to formation of a new island on an atomically flat (111) substrate/film surface, (b). An island edge ABCD grows by nucleation, (c), and growth, (d), of kinks.

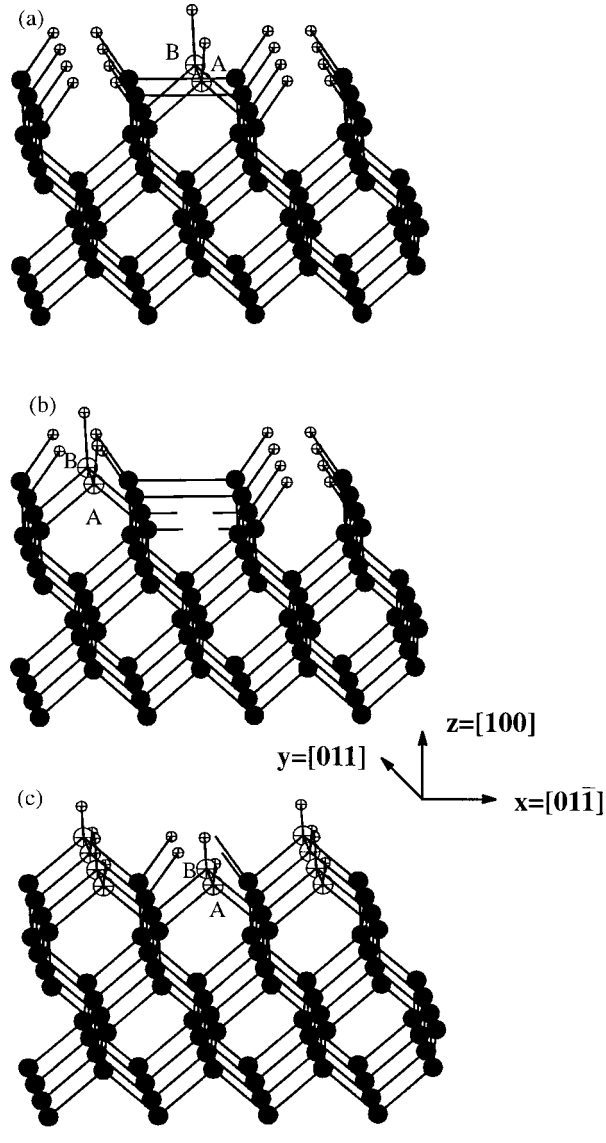

Figure 2 Nucleation (A) and the beginning of growth (B) of a new layer on an atomically flat (100)-oriented diamond film by the following mechanisms: (a) dimer insertion; (b) trough insertion and (c) by the BCN mechanism.

hydrocarbon molecule may take part in one of the possible surface reactions which leads to the incorporation of carbon atom from the hydrocarbon molecule into the diamond lattice and thus to film growth.

The film deposition is simulated by allowing the substrate to interact with a hot-filament heated process-gas containing various concentrations of H, H_2, CH_3, C_2H_2, etc in accordance with the set of surface chemical reactions reported in Table I of Part I [21]. The concentration of various gas-phase, surface and solid-phase species at the deposition surface is obtained by carrying out a reactor-scale modeling of CVD of the diamond films as reported in Part I [21].

In order to help interpret the results of atomic-scale modeling of the diamond deposition process, main surface phenomena accompanying the interaction between the reactive gas and the deposition surface are analyzed in this section.

A new layer on an atomically flat (111) plane is nucleated as a three-carbon bridge through a series of surface reactions as listed in Table I of Part I [21] culminating in reactions (1), (−5), (13), (21) (−25), (37), (29), (33) and (44). As shown in Fig. 1a there are three equivalent three-carbon bridge orientations. Carbon atoms forming the three-carbon bridges are represented as large crossed circles in Fig. 1a. The growth of either of these three bridges leads to formation of an island of the new layer, Fig. 1b. The edge of the island is marked as ABCD in Fig. 1b. The growth of the island takes place by nucleation and growth of the edge kinks. The nucleation of a new kink occurs by addition of two carbon atoms to the island edge as shown in Fig. 1c. Further growth of the kink entails the addition of one carbon atom at a time, Fig. 1d, and this is accomplished via the operation of the surface reactions, (1), (2), (13), 21), (25), (3), (−7) and (49), Table I of Part I [21].

A new layer on an atomically flat (100) plane can be nucleated (A) and subsequently grown (B) by one of the three mechanisms: (a) the dimer insertion, Fig. 2a; (b) the trough insertion, Fig. 2b and c the BCN mechanism, Fig. 2c. All three mechanisms are considered in the present work.

During deposition of the (111)-oriented single-crystalline diamond films various crystal defects of the point, line and plane type can form. Among the point-type defects, vacancies, Fig. 3a and entrapped hydrogen atoms, Fig. 3b, can be generated. Fig. 3c shows formation of a partial dislocation with the Burgers vector $b = a/6[121]$ which is accompanied with a stacking fault (a planar defect). Square and diamond symbols are used in Fig. 3c to indicate the carbon atoms residing on two adjacent $(\bar{1}01)$ planes each on one side of the stacking fault. Fig. 3d shows a (111)-type twin which is the result of nucleation and growth of a three-carbon bridge isomer on the atomically flat (111) surface.

In general, defects are less likely to form during growth of the (100)-oriented diamond films. In particular, significantly lower concentrations of the line and planar defects are generally observed in comparison with the ones in the (111)-oriented diamond films. Formation of the point defects is more likely and two types of such defects, vacancies and entrapped hydrogen atoms are shown in Figs 4a and b, respectively.

The kinetics of surface reactions is represented using the general formalism adopted in the Surface ChemKin computer program [22]. Within this formalism, the forward rate constant for reaction i, k_{f_i}, is assumed to be given by the following Arrhenius-type relation:

$$k_{f_i} = A_i T^{\beta_i} \exp\left(-\frac{E_i}{RT}\right) \tag{1}$$

where the pre-exponential factor A_i, the temperature exponent β_i and the activation energy E_i for all the surface reactions considered in the present work are obtained from Coltrin *et al*. [23, 24] and Battaile *et al*. [18], R is the universal gas constant and T is the absolute temperature. The reverse reaction rate constant is related to the forward reaction rate constant and can be computed using the procedure outlined in Appendix.

The temporal evolution of the diamond film during growth is modeled using the version of the kinetic Monte Carlo method recently developed by Battaile *et al*. [18]. Within this method, one surface reaction is allowed to take place at one surface site during each time step. The occurrence of one of the reactions at one of the sites is termed an event. At each time step, a list of all possible events is constructed and the probability for each event is set proportional to the rate of the associated surface reaction relative to the rates of the surface reactions associated with all the other possible events. Computer implementation of kinetic Monte Carlo method is discussed in considerable details in Part I [21] and hence it will not be discussed here.

As discussed in Part I [21], the present Monte Carlo method uses a variable time increment which adjusts itself dynamically and stochastically to account for the fact that different events take place at different rates.

2.2. Results

The top view of an (111)-oriented diamond film deposited under the CVD conditions typical for a rotating-disk hot-filament reactor: reactive gas at the reactor inlet (0.4% CH_4, 92.6% H_2), $T_{\text{heator}} = 2000$ K, $T_{\text{substrate}} = 1000$ K, $p = 20.25$ Torr, Heater-to-Substrate distance $= 1.3$ cm at four deposition times is shown in Fig. 5a–d. The surface morphology shown in these figures is typical for the (111)-oriented diamond films. To help the analysis of surface morphology, different shades of grey are used to designate the relative magnitude of the z coordinate of the atoms. The white (the brightest shade of grey) atoms are located on the very top of the surface asperities, while the black (the darkest shade of grey) ones are located on the bottom of the surface valleys. To further improve the clarity of the surface morphology, the regions containing (111) twins are represented using circles of somewhat larger diameter. At short simulation times, Fig. 5a, there is a relatively large fraction of twins (T) separated from the regular regions by dislocations loops (D) and gaps (G). As discussed earlier, formation of a new (111) layer starts with formation of a three-carbon bridge (B, Fig. 5b), which as it grows forms first a nucleus (N) and then a large

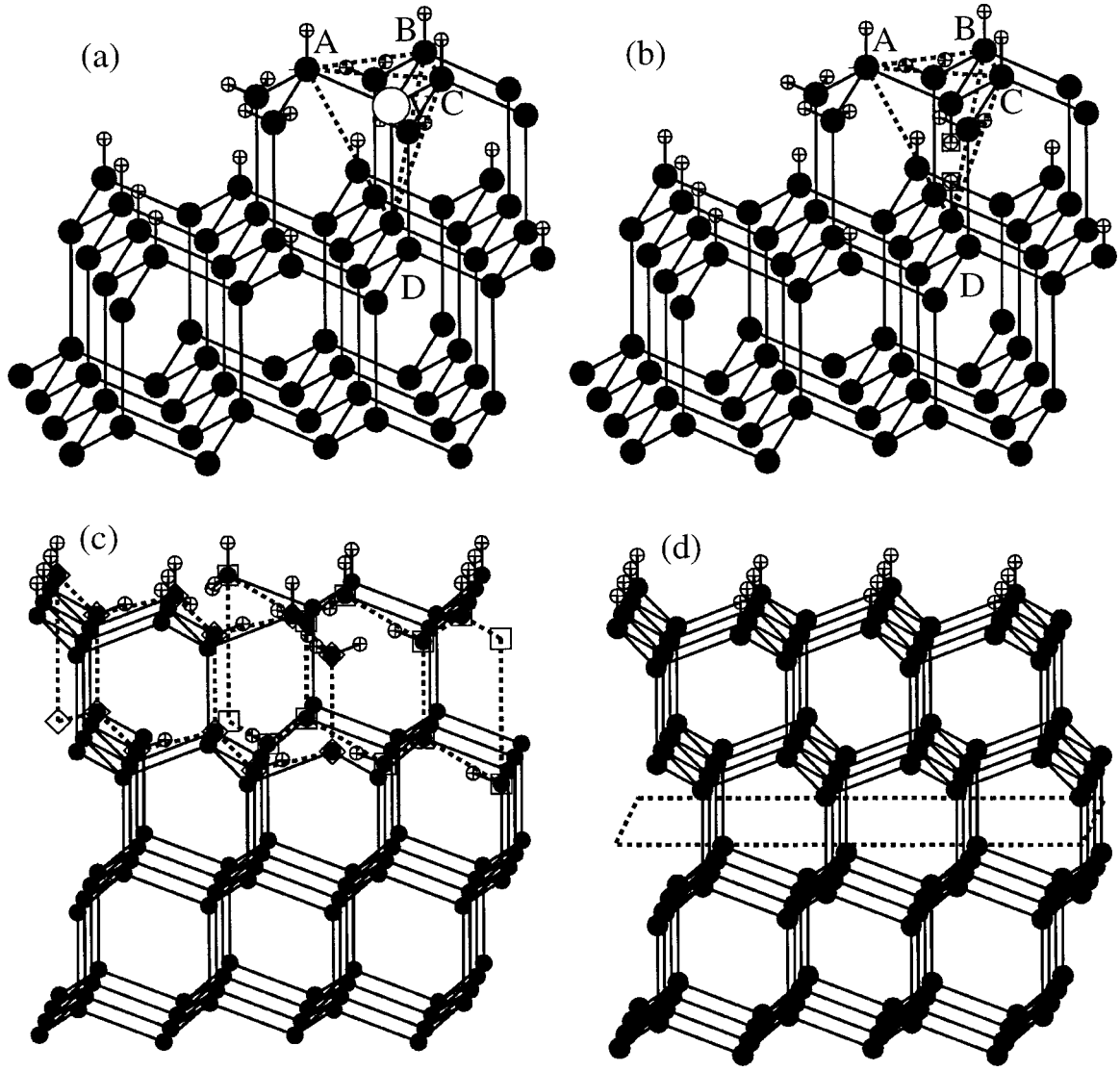

Figure 3 Crystal defects whose formation is allowed during the atomic-scale simulations of CVD of the (111)-oriented diamond films: (a) a vacancy (V); (b) entrapped hydrogen atoms (small circles surrounded by a square); (c) a partial dislocation with the Burgers vector $b = a/6[1\bar{2}1]$ and the associated stacking fault (marked by two parallel adjacent $(\bar{1}01)$ planes, one denoted by diamond and the other by square symbols); (d) a (111) twin. The basic diamond tetrahedron ABCD is outlined using dashed lines in (a) and (b).

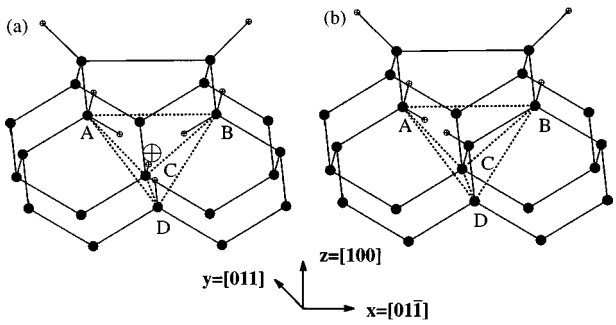

Figure 4 Formation of (a) a vacancy (the large crossed circle) and (b) a pair of entrapped hydrogen atoms (two small crossed circles) in an (100)-oriented diamond film. Dashed lines are used to designate the basic diamond tetrahedron which contains the point defect.

island (I). Large islands, I_1 and I_2 in Fig. 5b and c are bounded by the well defined edges (E) and kinks (K). The evolution of the morphology of the islands, I_1 and I_2, with time, Fig. 5b and c, clearly shows that kink nucleation and motion is the main mechanism of island growth. The edge/kink morphology of the islands persists even after isolated islands coalesce, Fig. 5d. Since the regular regions constitute the major portion of the film surface, they are more likely to nucleate a new (111)-layer and hence they grow faster than the twinned regions. Thus, the twinned regions are gradually being covered with the regular regions (C), and become buried inside the film.

A side view of the four (111)-oriented diamond films corresponding to Fig. 5a–d is shown in Fig. 6a–d. For comparison, all the morphological features marked in Fig. 5a–d, are also indicated in Fig. 6a–d. These figures clearly show that the growth of (111)-oriented diamond films is dominated by the edge/kink-type of growth of (111)-islands. In other words, the growth of the existing (111) islands appears to be a faster process than the process of nucleation of new (111) islands. Consequently, the surface morphology of the (111)-oriented diamond films is dominated by (111) terraces and steps.

The effect of substrate temperature (the remaining processing conditions kept identical to the ones listed above) on the (111)-oriented film deposition rate is shown in Fig. 7a. For comparison the experimental

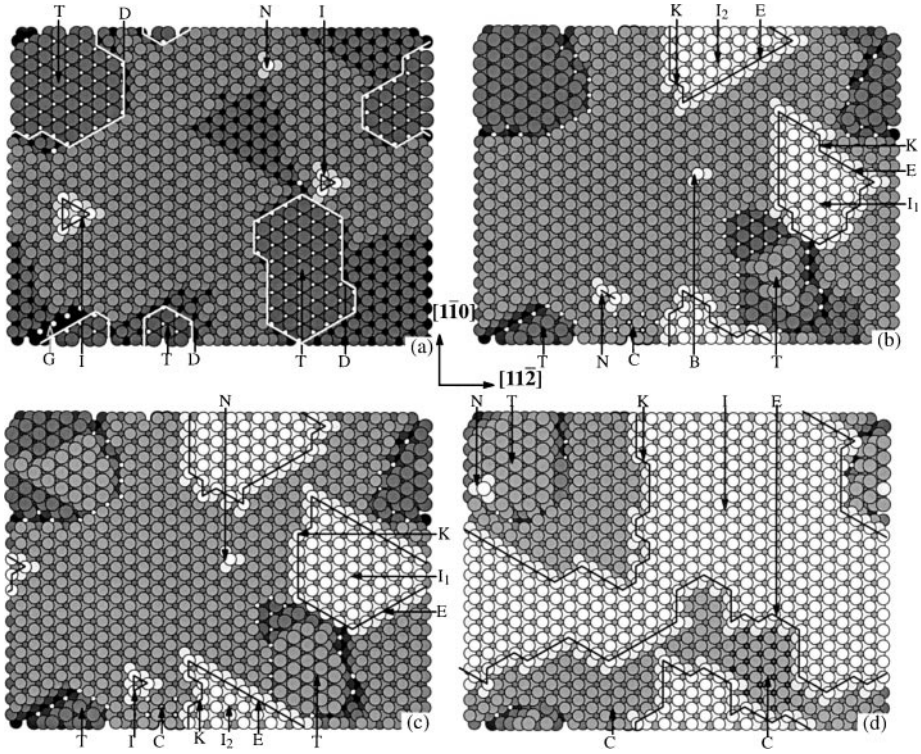

Figure 5 Top view of an (111)-oriented diamond film obtained under the following CVD conditions in the reactor: Reactive gas at the reactor inlet (0.4% CH_4, 92.5% H_2), $T_{heator} = 2000$ K, $T_{substrate} = 1000$ K, $p = 20.25$ Torr, Heater-to-Substrate Distance $= 1.3$ cm. Deposition times: (a) 0.87 s; (b) 1.81 s; (c) 2.07 s and (d) 2.85 s. Nomenclature: B - 3-carbon bridge, C - Twin covered by regular crystal, D - Dislocation loop, E - Edge, G - Gap, I - Island, K - Kink, N - Nucleus, T - Twin, V - Void.

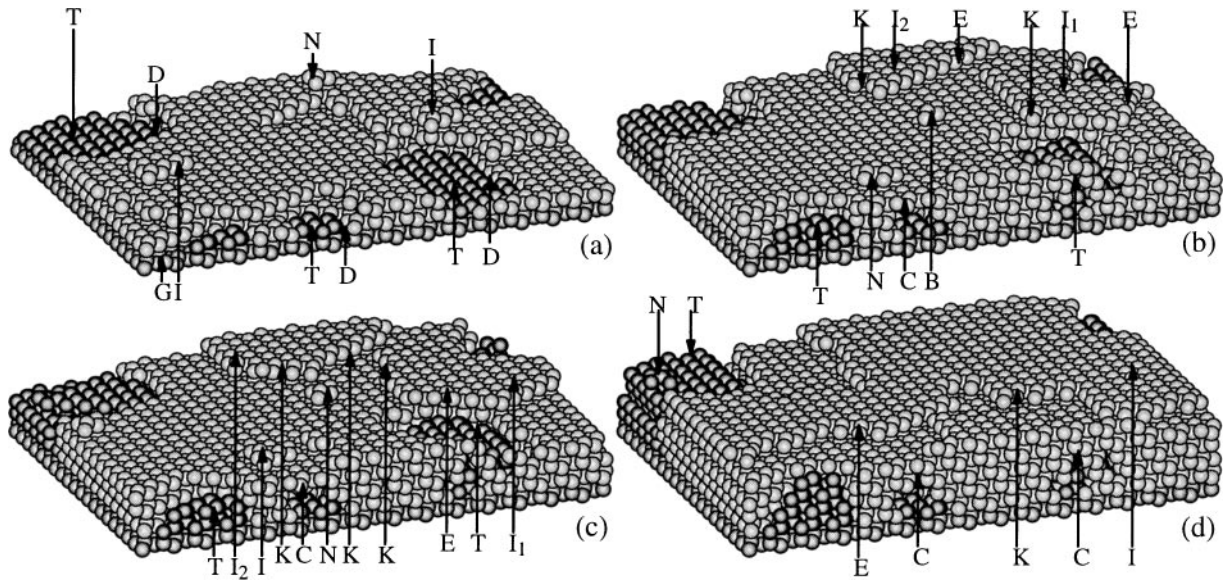

Figure 6 The side view of the four (111)-oriented diamond films shown in Fig. 5a–d.

results of Chu *et al*. [25] are also shown in Fig. 7a. The agreement between the two sets of results can be considered as reasonable.

The effect of substrate temperature on the concentration of point-type defects (vacancies and entrapped hydrogen atoms) and the area fraction of twins in the (111)-oriented diamond films are shown respectively in Fig. 8a and b. The concentration of the point-type defects is found to be fairly constant during the deposition process, Fig. 8a. In sharp contrast the twinned fraction of the film is found to monotonically decrease with the film thickness, Fig. 8b.

The results depicted in Figs 7 and 8 show that both the growth rate of the (111)-oriented diamond films and the concentrations of crystalline defects/imperfections increase with the substrate temperature. This suggests that there is an intermediate temperature range within which one can obtain an optimum combination of the film quality and the high rate of deposition. This temperature can be determined by first defining a parameter in which the film growth rate and the inverse concentration of the defects are properly weighted and then identifying the temperature at which such a parameter acquires a maximum value. Since the relative weighting factors

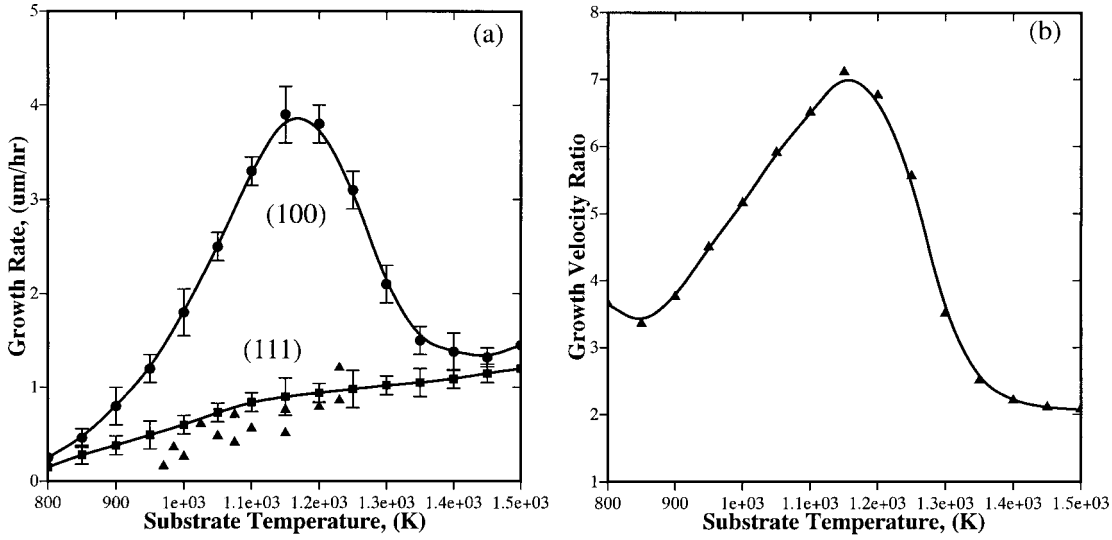

Figure 7 Effect of the substrate temperature on the deposition rate of (111)- and (100)-oriented diamond films, (a), and the corresponding growth velocity ratio α_{3D}, (b), under the CVD conditions given in Fig. 5. Error bars represent on standard deviation over five simulation runs.

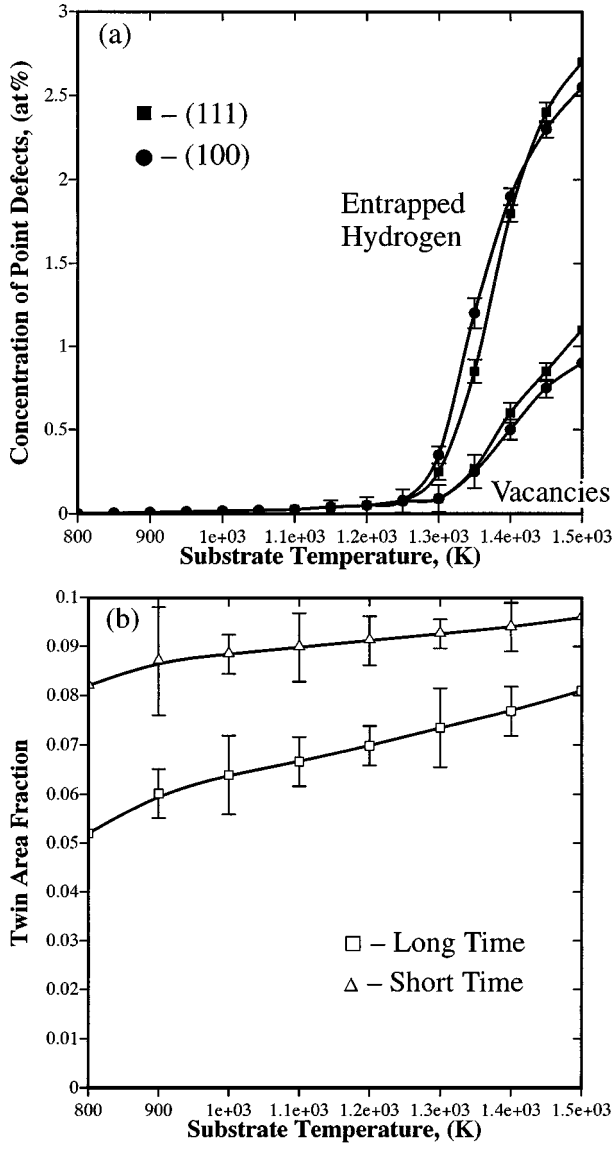

Figure 8 Effect of the substrate temperature on the concentration of vacancies and entrapped hydrogen atoms in (111)- and (100)-oriented diamond films, (a), and twins in (111)-oriented diamond films, (b), under the CVD conditions specified in Fig. 5. Error bars represent on standard deviation over five simulation runs.

for the film growth rate and the inverse concentration of the defects are a function of the application of the diamond film, identification of the optimum substrate temperature is not carried out in the present work.

The top view of an (100)-oriented diamond film deposited under the identical condition as the (111)-oriented diamond film discussed above is shown in Fig. 9a–d. In order to indicate formation of dimer bonds along the [011] direction, the distance between the carbon atoms forming a dimer bond is shortened. A striking feature of the surface morphologies shown in Fig. 9a–d is the absence of well defined regularly-shaped islands surrounded with straight edges and kinks. Instead, typical islands, I_1, I_2, I_3 in Fig. 9b and c, are quite irregular in shape and the film growth appears to be affected both by the nucleation of new islands and the growth of the existing ones. Consequently, the film surface remains quite irregular during the deposition. At large simulation times, surface irregularities result in the formation of deep pits P which can be observed in Fig. 9d. A careful analysis of the deposited surface in Fig. 9a–d reveals that all three deposition mechanisms: the dimer insertion (D), the trough insertion (T) and the BCN mechanism (B) are found to be operative. The relative contributions of these mechanisms is estimated as $D:T:B \cong 16:7:6$ and appear to be fairly constant during the deposition.

The side view of the four (100-oriented diamond films corresponding to Fig. 9a–d is shown in Fig. 10a–d. For comparison, all the morphological features marked in Fig. 9a–d, are also indicated in Fig. 10a–d. The side views of the (100)-oriented films further demonstrate a pronounced roughness of the film surface.

The effect of substrate temperature on the (100)-oriented film deposition rate is shown in Fig. 7a. The results indicate that there is an intermediate temperature range within which the deposition rate is maximum.

The effect of substrate temperature on the concentration of vacancies and entrapped hydrogen atoms in the (100)-oriented diamond films is shown in Fig. 8a. Since the concentration of the defects increases with

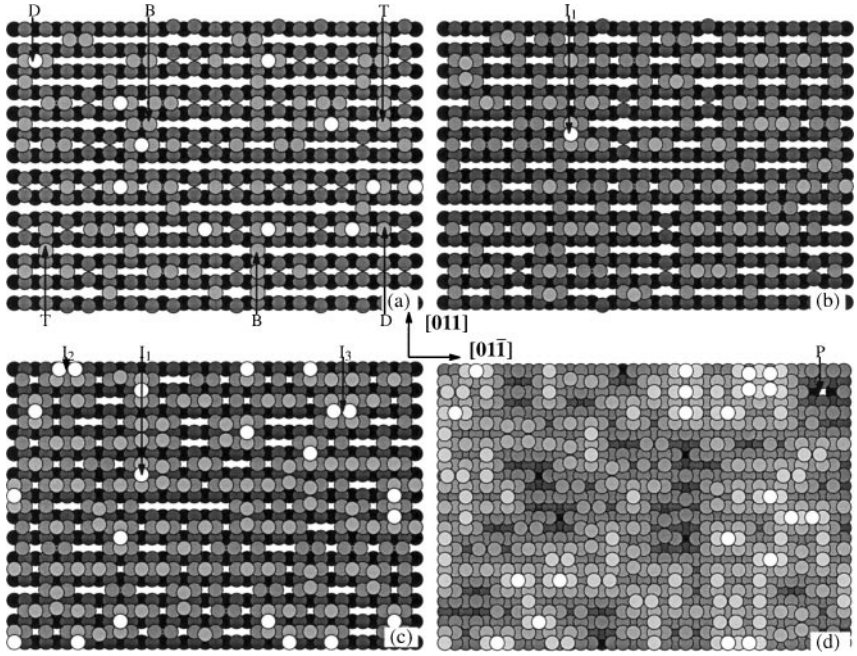

Figure 9 Top view of four (100) surface configurations obtained under the CVD conditions identical to the ones listed in Fig. 5. Deposition times: (a) 0.01 s; (b) 0.018 s; (c) 0.032 s and (d) 0.208 s. Nomenclature: B—BCN mechanism, D—Dimer insertion mechanism, P—Pit, I—Island, T—Trough insertion mechanism.

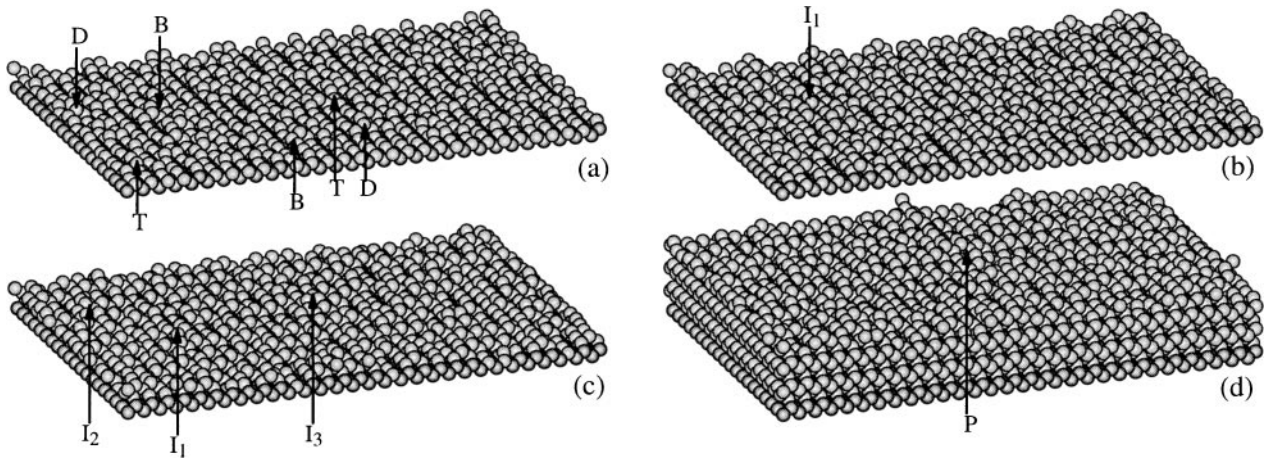

Figure 10 Side view of the four (100)-oriented diamond films shown in Fig. 9a–d.

the substrate temperature and the deposition rate is maximum at a temperature around 1150 K, there is again a intermediate temperature range within which CVD is optimal relative to achieving a maximum deposition rate and a minimum concentration of the defects.

3. Grain-scale modeling of CVD

3.1. General consideration

In this section, the growth of polycrystalline CVD-grown diamond films at the grain scale is analyzed using both a simple three-dimensional and a two-dimensional (a Van der Drift-type) model. It is well-established that the surface of polycrystalline diamond films is faceted with the (111) and, to a less extent, (100) crystallographic planes. The growth rates of these facets are assumed to be equal to the rates of the (111)- and (100)-oriented single-crystalline diamond films determined in the previous section.

Grain-scale modeling of CVD of diamond films is first carried out using a simple four square-grain structure. A top view of the four-grain film is shown in Fig. 11. Grains 1 and 4 have a ⟨100⟩ direction normal to the substrate while grains 2 and 3 have a ⟨110⟩ direction normal to the substrate. The surface of grains 1 and 4 is composed entirely of the (111) facets while the surface of grains 2 and 3 is composed of both the (111) and (100) facets. The four-grain film was chosen in order to account for the experimental findings which show that the surface of polycrystalline diamond films is predominantly composed of the (111)-type facets and, to a lower extent, of the (100)-type facets. Following the procedure described below, x, y and z components of the velocity of each grain vertex are calculated. During calculation of the vertex velocity, the effect of the inclination of each surface facets relative to the plane of the substrate on the facet growth rate is taken into account. This is done by multiplying the deposition rate of each surface facet by a factor β_0 which is proportional

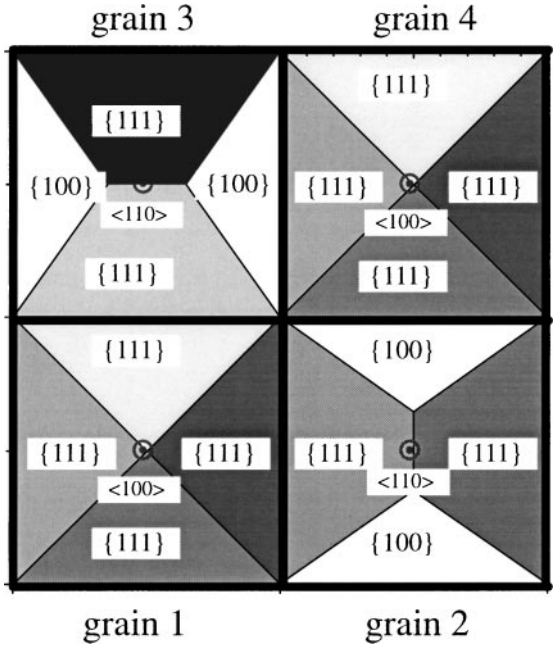

Figure 11 Top view of the four-grain structure used in three-dimensional simulations of the diamond film growth. (uvw) notation used to denote the orientation of grains facets and ⟨*hkl*⟩ the crystallographic direction normal to the substrate surface. Heavy lines are used to denote the grain boundaries.

to the deposition flux per unit facet area. Under the assumption of a uniform distribution of the incident particles, $\beta_0 = \cos\alpha_0$, where α_0 is the angle between the facet normal and the substrate plane normal. For the four-grain film, the following α_0 values are determined: 54.75° for the (111)-facets on grains 1 and 4 and 35.26° for the (111)-facets and 45° for the (100)-facets on grains 2 and 3.

As will be shown below the morphology of the film is governed by the relative magnitude of the (111) and (100) growth rates which is conveniently expressed using a growth velocity ratio:

$$\alpha_{3D} \equiv \sqrt{3}\frac{v_{100}}{v_{111}} \tag{2}$$

where v_{100} and v_{111} are the growth rates of the (100) and (111) facets, respectively. It can be easily verified that the ultimate shape of an isolated three-dimensional nucleus is determined by the magnitude of α_{3D}. Specifically for $\alpha_{3D} \leq 1$, the nucleus adopts a cubic shape surrounded by the (100) facets. For $\alpha_{3D} \geq 3$, on the other hand, the nucleus becomes an (111)-faced octahedron. For $1 < \alpha_{3D} < 3$, the nucleus acquires a (100)-(111)-faced cubo-octahedron. The variation of the growth velocity ratio α_{3D} with the substrate temperature under the remaining CVD processing conditions given in the previous section is shown in Fig. 7b.

The growth of polycrystalline diamond films at the grain-scale level is also analyzed using a two-dimensional idealization in which the surface of a in-plane projected diamond film is taken to be composed of projected (111) and (100) facets and projected [110] edges. Modeling of the evolution of the film grain-structure follows closely the approach initially proposed by Van der Drift [20]. At the beginning of a simulation, diamond nuclei in the shape of triangles and quadrilaterals are generated at random. In accordance with the morphology of the four-grain film used in the previous section, three types of nuclei shown in Fig. 12 are considered. The nuclei are next allowed to grow by the outward motion of their edges. The growth process is modeled by determining the velocity v of each vertex of the nucleus, and allowing the vertex to move by a distance $v\Delta t$ where Δt is a small time increment. The procedure used for determination of the velocity components of a vertex is explained schematically in Fig. 12. The velocities $v_{\rm l}$ and $v_{\rm r}$ of the nucleus edges to the left and to right of vertex A are first used to find their contributions to the velocity of vertex A, ${v_{\rm l}}^{\rm A}$ and ${v_{\rm r}}^{\rm A}$, respectively. Then ${v_{\rm l}}^{\rm A}$ and ${v_{\rm r}}^{\rm A}$ are next summed as vectors to obtain the vertex velocity, v. Finally, v is resolved into its x and y components, v_x and v_y. This procedure yields the following relations between v_x, v_y and $v_{\rm l}$, $v_{\rm r}$.

$$v_x = \frac{v_{\rm l}\cos\beta + v_{\rm r}\cos\alpha}{\sin(\alpha - \beta)} \tag{3}$$

$$v_y = \frac{v_{\rm l}\sin\beta + v_{\rm r}\sin\alpha}{\sin(\alpha - \beta)} \tag{4}$$

where α and β, as indicated in Fig. 13, are respectively the angles the left and the right edges of vertex A make with the positive side of the x axis.

Initially, the nuclei grow independently from each other. However after certain simulation time, the nuclei have grown to the extent that they begin to contact with their neighbors, ultimately forming a continuous film at the substrate. Subsequent growth of the film is accompanied by a competition between the adjacent grains, the process in which more favorably oriented grains (the grains whose direction of the fastest growth is nearly normal to the surface of the substrate) block off the growth of less favorably oriented grains. As a result of this "evolutionary selection" process, the number of grains becomes smaller than the number of nuclei and the film acquires a familiar columnar-grain structure.

3.2. Results

Fig. 3a and b show the evolution of the surface structure in the four-grain film under the periodic boundary condition in the x and y directions for $\alpha_{3D} = 2.0$. These results are typical for $\alpha_{3D} > 1.5$. As the film grows, the (100) facets shrink as grains 2 and 3 begin to cover and block off grain 4. Meanwhile, the grain-1/grain-2 and grain-1/grain-3 boundaries extend only in the z direction. After certain simulation time, the (100) facets disappear. This finding is, at least, qualitatively consistent with the results of Wild *et al*. [26] which show that the ⟨110⟩ texture (resulting from the growth of grains 2 and 3) increases with the film thickness. In addition, a relatively low stacking fault energy promotes the tendency for formation of twins on the (111) surface facets which can further contribute to an increase in the ⟨110⟩ texture of polycrystalline diamond films. This can be explained as following. When a twin is formed, the crystal lattice is rotated about the twin-plane normal n

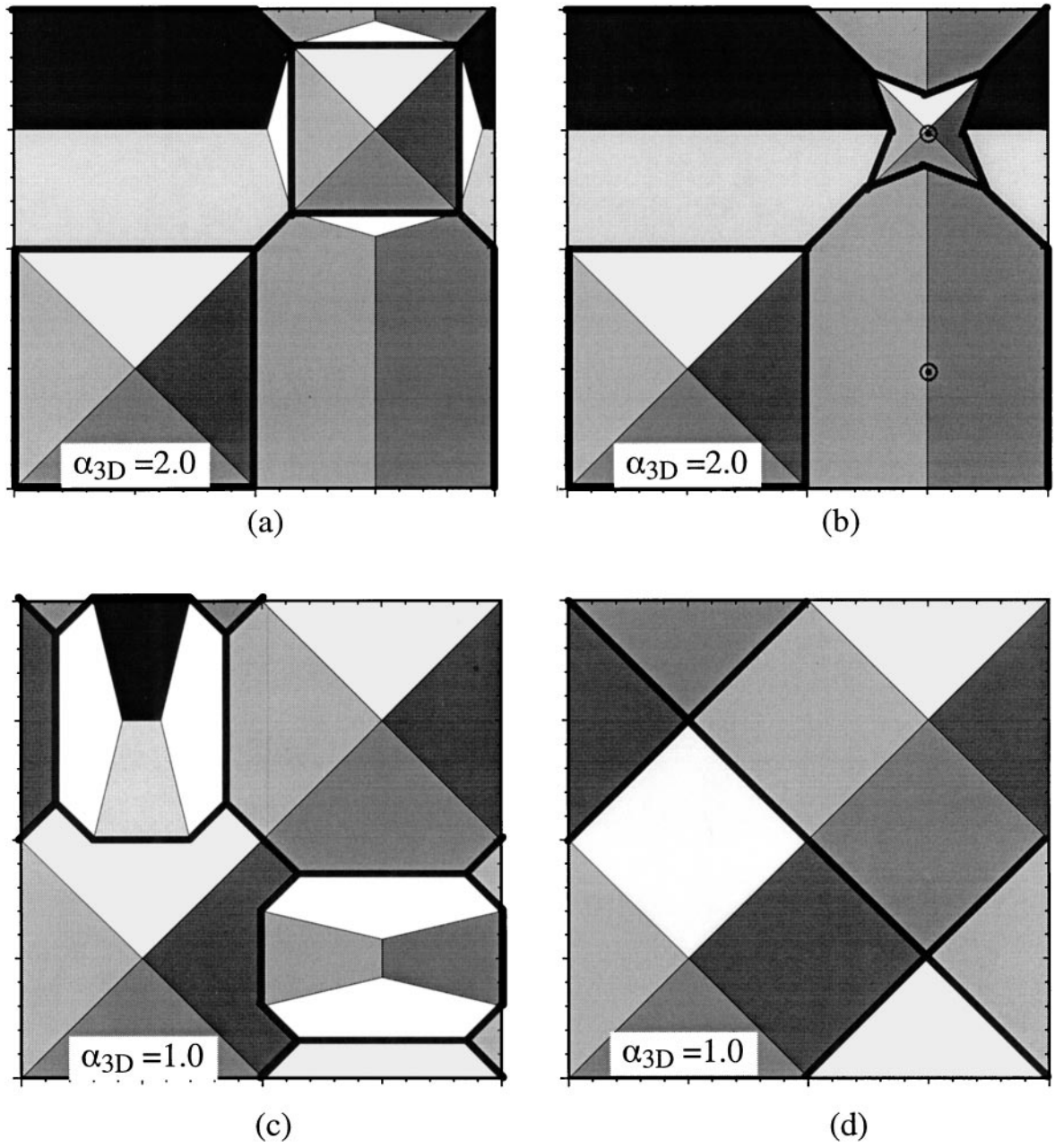

Figure 12 An intermediate, (a), and the final, (b), top-view configuration of the four-grain structure under the deposition conditions corresponding to $\alpha_{3D} = 2.0$; (c) and (d) are the corresponding top views for $\alpha_{3D} = 1.0$.

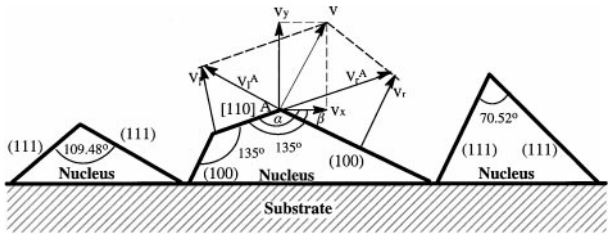

Figure 13 A Schematic of three types of two-dimensional nuclei and the vertex velocity construction procedure used in the Van der Drift analysis of the diamond film growth.

by 180°. This rotation is represented by the following rotation matrix:

$$R = 2nn^{\mathrm{T}} - I \tag{5}$$

where n is expressed as a (3×1) vector, n^{T} is its transpose and I is the second order identity matrix. In the present case $n^{\mathrm{T}} = 1/\sqrt{3}\langle 111\rangle$ and there are four $\langle 111\rangle$ plane normals. Twinning causes any lattice vector v to become $R_{\mathrm{twin}}v$. In the case of grains 1 and 4, twinning on each of the four (111) planes causes the direction normal to the film substrate to change from $\langle 100\rangle$ to $\langle 122\rangle$. Conversely, for grains 2 and 3, twinning on two (111) planes causes the direction normal to the substrate, $\langle 110\rangle$, to change to a $\langle 114\rangle$ direction while twinning on the other two (111) planes retains the $\langle 110\rangle$ texture of these grains. This analysis indicates that even if the grain-1/grain-2 and grain-1/grain-3 boundaries in Fig. 12b are to remain vertical and hence grain 1 retains its original size during the film growth, the $\langle 110\rangle$ texture would increase relative to the $\langle 100\rangle$ texture.

Fig. 13c and d show the evolution of the surface structure in the four-grain diamond film under the growth velocity ratio of $\alpha_{3D} = 1.0$. These results are typical for $\alpha_{3D} < 1.5$. As shown in Fig. 13c, both the (111)

and the (100) facets on grains 2 and 3 shrink and ultimately disappear as grains 2 and 3 are being covered and finally completely blocked-off by grains 1 and 4. This findings suggest that under the conditions corresponding to $\alpha_{3D} < 1.5$, the film surface is completely covered with (111) facets and the film has a ⟨100⟩-type texture. It should be noted, however, that based on our atomic-scale simulation results shown in Fig. 7b, the growth velocity ratio is generally greater than 1.5 under the CVD processing conditions. Therefore, ⟨100⟩-textured polycrystalline diamond films are not expected to be obtained under the typical CVD conditions. This finding is in agreement with the experimental results of Wild *et al*. [26].

Fig. 14a and b show the evolution of the grain structure, surface morphology/roughness and texture in CVD-grown polycrystalline diamond films under the processing condition corresponding to the growth velocity ratio $\alpha_{3D} = 2.0$ and $\alpha_{3D} = 1.0$, respectively. These results are typical for $\alpha_{3D} > 1.5$ and $\alpha_{3D} < 1.5$, respectively.

For $\alpha_{3D} > 1.5$, Fig. 14a, the film surface is completely covered with (111)-type facets while surface asperities are predominantly the ⟨110⟩-edges (lines of intersections of two (111) planes). As a result, the film surface is quite smooth at the grain-size scale and the film acquires a ⟨110⟩-type texture. All these findings are fully consistent with the experimental results of Wild *et al*. [26].

For $\alpha_{3D} < 1.5$, Fig. 14b, the surface is also composed entirely of the (111) facets but it is quite rough at the grain-size scale. Furthermore, in sharp contrast to the $\alpha_{3D} > 1.5$ case, surface asperities correspond to the diamond-octahedron vertices (the points of intersection of four (111)-planes) rather than to the diamond-octahedron vertices. The film acquires a ⟨100⟩-type texture, the intensity of which increases as the film grows.

The results shown in Fig. 14a and b suggest that, from the standpoint of obtaining a smoother film surface, it is advantageous to employ the CVD conditions correspond to $\alpha_{3D} > 1.5$. In addition, the film deposition rate for the $\alpha_{3D} > 1.5$ case is found to be about 12–15% higher than that in the $\alpha_{3D} < 1.5$ case. This could be seen in Fig. 14a and b in which the final films structures correspond to the same deposition times.

4. Discussion and conclusions

In the present work, chemical vapor deposition of polycrystalline diamond films is analyzed by combining an atomic-scale model with two grain-scale models. In such analysis, the atomic-scale model enables determination of intrinsic growth rates of the surface facets of polycrystalline films and the effect of surface conditions on the rate of incorporation of the crystalline defects. The grain-scale models, on the other hand allow determination of the polycrystalline film growth rate and surface roughness, grain-structure and crystallographic texture in the as-deposited polycrystalline films.

In Part I of this two-part paper [21], a reactor-scale model and the present atomic-scale model were combined to establish the relationships between CVD-processing parameters such as the concentration of species in the feed gas temperature and pressure and the chemical and thermal conditions at the film surface. Thus, by combining the analysis presented in Part I with the one presented in this paper, one can establish a direct link between the processing conditions and the resulting microstructure (and properties) of the as-deposited films. Such a link can be used to both optimize the process (Process Design) and/or improve the performance of the deposited film (Product Design).

Acknowledgements

The work presented here has been supported by the U.S. Army Research Office, Grant DAAH04-96-1-0197 and

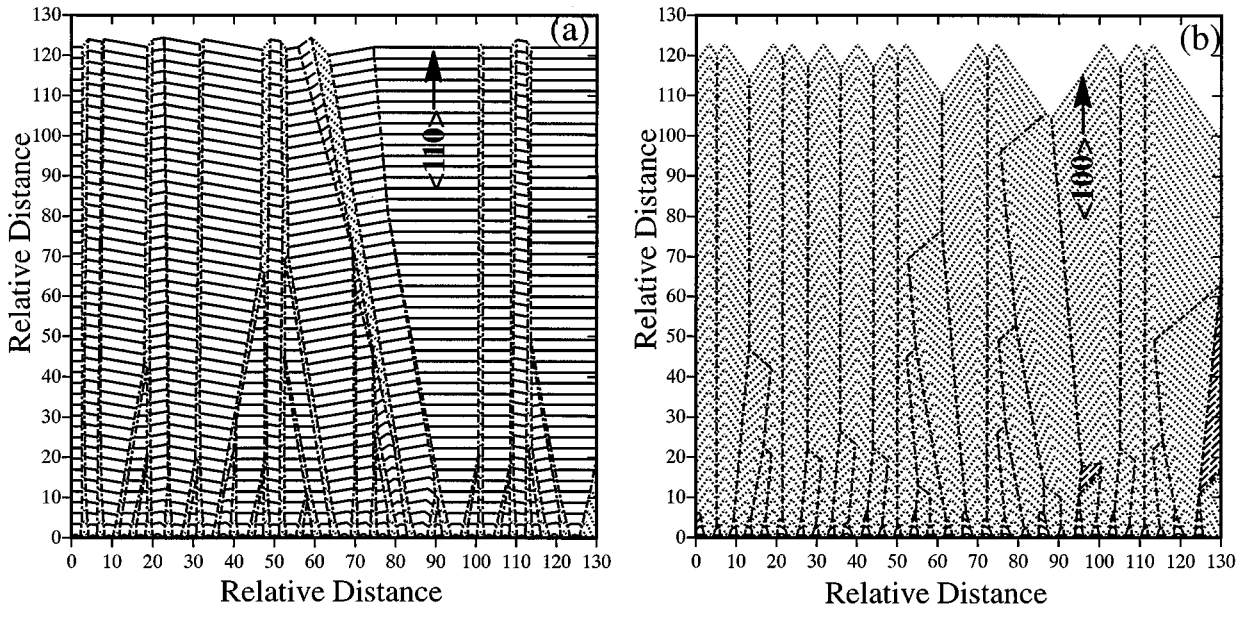

Figure 14 The evolution of two-dimensional grain structure during CVD of polycrystalline diamond films under the conditions corresponding to the growth velocity ratio: (a) $\alpha_{3D} = 2.0$ and (b) $\alpha_{3D} = 1.0$. Nomenclature: Solid lines - {110} edges; dotted lines - projected {111} facets; dash-and-dot lines - grain boundaries.

Grant DAAD19-99-1-0096. The authors are indebted to Dr. David M. Stepp of ARO for the continuing interest in the present work. Encouragement and friendship of Professor R. J. Diefendorf is greatly appreciated. The authors also acknowledge the support of the Office of High Performance Computing Facilities at Clemson University.

Appendix: Computation of the reverse reaction rate constant

The reverse reaction rate constant, k_{ri}, is related to the forward reaction rate constant as:

$$k_{r_i} = \frac{k_{f_i}}{K_{C_i}} \tag{A1}$$

where K_{C_i} is the equilibrium reaction constant expressed in concentration units and is related to the equilibrium constant expressed in pressure units, K_{P_i} as:

$$K_{P_i} = K_{C_i}\left(\frac{P_{\text{atm}}}{RT}\right)^{-\sum_{k=1}^{K_g} v_{ki}} \prod_{n=N_s^f}^{N_s^l} \left(\Gamma_n^0\right)^{-\sum_{k=K_s^f(n)}^{K_s^l(n)} v_{ki}} \prod_{k=K_s^f(n)}^{K_s^l(n)} \sigma_k^{v_{ki}} \tag{A2}$$

where P_{atm} is the pressure of 1 atm, Γ_n^0 the standard state density of the surface sites of type n, $\sigma_k(n)$ the number of sites of type n occupied by species k, and v_{ki}'s are the stoichiometric reaction coefficients associated with species k and reaction i, K_g the total number of gas species and $K_s^f(n)$ and $K_s^l(n)$ the first and the last surface species residing on n-type sites, respectively, and N_s^f and N_s^l the first and the last surface site types, respectively.

K_{P_i} can be computed from the standard-state enthalpy change ΔH_i^0 and the standard-state entropy change ΔS_i^0 accompanying reaction i as:

$$K_{P_i} = \exp\left(\frac{\Delta S_i^0}{R} - \frac{\Delta H_i^0}{RT}\right) \tag{A3}$$

ΔH_i^0 and ΔS_i^0 for the set of surface reactions used in the present work are obtained from Coltrin *et al.* [23, 24] and Battaile *et al.* [18].

It should be noted that for the surface reactions listed in Table I of Part I [21] in which the number of surface species is conserved, the sum $\sum_{k=1}^{K_g} v_{ki} = 0$, and hence $(P_{\text{atm}}/RT)\sum_{k=1}^{K_g} v_{ki} = 1$. For the remaining surface reactions $\sum_{k=1}^{K_g} v_{ki} = -1$ and, hence $(P_{\text{atm}}/RT)\sum_{k=1}^{K_g} v_{ki} = 0.0122 \frac{K}{\text{cm}^3}\frac{1}{T}$.

References

1. K. E. SPEAR, *J. Amer. Ceram. Soc.* **72** (1989) 171.
2. J. E. BUTLER and R. L. WOODIN, *Philos. Trans. R. Soc. London, Ser. A* **342** (1993) 209.
3. D. G. GOODWIN and J. E. BUTLER, in "Handbook of Industrial Diamonds and Diamond Films," edited by M. A. Prelas, G. Popovici and L. K. Bigelow (Dekker, New York, 1997) p. 527.
4. M. E. COLTRIN, R. J. KEE and G. H. EVANS, *J. Electrochem. Soc.* **136** (1989) 819.
5. M. E. COLTRIN, R. J. KEE and F. M. RUPLEY, *International J. of Chemical Kinetics*, **23** (1991) 111.
6. D. W. BRENNER, *Phys. Rev. B* **42** (1990) 9458.
7. B. J. GARRISON, E. J. DAWNKASKI, D. SRIVASTAVA and D. W. BRENNER, *Science* **255** (1992) 835.
8. D. HUANG and M. FRENKLACH, *J. Phys. Chem.* **96** (1992) 1868.
9. V. I. GAVRILENKO, *Phys. Rev. B* **47** (1993) 9556.
10. Y. L. YANG and M. P. D'EVENLYN, *J. Amer. Chem. Soc.* **114** (1992) 2796.
11. T. FRAUENHWIM, U. STEPHAN, P. BLAUDECK, D. POREZAG, H.-G. BUSMANN, W. ZIMMERMANN-EDLING and S. LAUER, *Phys. Rev. B* **48** (1993) 18189.
12. Z. JING and J. L. WHITTEN, *Surf. Sci.* **314** (1994) 300.
13. S. SKOKOV, C. S. CARMER, B. WEINER and M. FRENKLACH, *Phys. Rev. B* **49** (1994) 5662.
14. S. CIRACI and I. P. BATRA, *ibid.* **15** (1977) 3254.
15. S. F. YANG, D. A. DRABOLD and J. B. ADAMS, *ibid.* **48** (1993) 5261.
16. B. N. DAVIDSON and W. E. PICKETT, *ibid.* **49** (1994) 11253.
17. M. M. CLARK, L. M. RAFF and H. L. SCOTT, *Comput. Phys.* **10** (1996) 584.
18. C. C. BATTAILE, D. J. SROLOVITZ and J. E. BUTLER, *J. Appl. Phys.* **82**(12) (1997).
19. M. GRUJICIC and S. G. LAI, *Journal of Material Science*, **34** i1, (1999) 7.
20. A. VAN DER DRIFT, *Philips Res. Rep.*, **22** (1967) 267.
21. M. GRUJICIC and S. G. LAI, *Journal of Material Science*, submitted.
22. SURFACE CHEMKIN III, User Manual, Sandia National Laboratories, San Diego, CA 1996.
23. M. E. COLTRIN and D. S. DANDY, *J. Appl. Phys.* **74**(9) (1993) 5803.
24. D. S. DANDY and M. E. COLTRIN, *J. Mater. Res.*, **10**(8) (1995) 1993.
25. C. J. CHU, R. H. HAUGE, J. L. MARGRAVE and M. P. D'EVELYN, *Appl. Phys. Lett.* **61** (1992) 1393.
26. CH. WILD, N. HERRES and P. KOIDL, *J. Appl. Phys.* **68**(3) (1990) 973.

Received 12 August 1999
and accepted 30 March 2000